

A Pair of Rare Three-Dimensional Chiral Polyoxometalate-Based Metal–Organic Framework Enantiomers Featuring Superior Performance as the Anode of Lithium-Ion Battery

Weiwei Cheng,^{†,§,⊥} Feng-Cui Shen,^{†,‡,||,⊥} Yun-shan Xue,[†] Ximing Luo,[†] Min Fang,[‡] Ya-Qian Lan,^{*,‡,⊥} and Yan Xu^{*,†,⊥}

[†]College of Chemistry and Chemical Engineering, State Key Laboratory of Materials-Oriented Chemical Engineering, Nanjing Tech University, Nanjing 210009, People's Republic of China

[‡]Department of Chemistry, School of Chemistry and Materials Science, Nanjing Normal University, Nanjing 210023, People's Republic of China

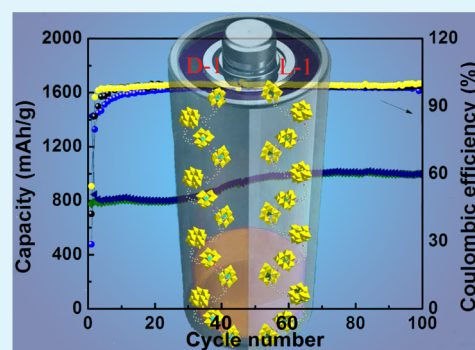
[§]School of Chemistry and Bioengineering, Nanjing Normal University Taizhou College, Taizhou 225300, People's Republic of China

^{||}College of Biological and Chemical Engineering, Anhui Polytechnic University, Wuhu, 241000, People's Republic of China

Supporting Information

ABSTRACT: Two rare three-dimensional (3D) chiral polyoxometalate-based metal–organic framework (POMOF) materials, D-[PMo₈VMo₄O₃₇(OH)₃Zn₄][BPP]₂·2[pyridine]·H₂O (D-1) and L-[PMo₈VMo₄O₃₇(OH)₃Zn₄][BPP]₂·2[pyridine]·H₂O (L-1) (BPP = 1,3-bis-(4-pyridyl)propane) were prepared with achiral ligand under solvothermal conditions. They are the first 3D chiral POM-based frameworks based on a Zn-ε-Keggin unit and achiral ligands. The CD spectra and structural analyses indicate that the two polyoxometalate-based metal–organic frameworks are enantiomers. The alternate connection of Zn-ε-Keggin cluster and BPP ligands generate helical infinite chains, while each single spiral chain is further interlinked to adjacent neighboring units to produce a 3D regular ordered chiral architecture with a qtz topology. Compound 1 (mixtures of D-1 and L-1) exhibited excellent stability in both acid and base aqueous solutions. When compound 1 was used as an anode electrode material of rechargeable Li-ion batteries (LIBs), outstanding reversible capacity of 1004 mA h g^{−1} was obtained after 100 cycles along with cycle stability and outstanding rate performance. Such a high reversible capacity has previously never been reported for the LIB anodes within the pristine POM-based crystals.

KEYWORDS: polyoxometalate, metal–organic framework, lithium-ion battery, enantiomer, anode electrode material



Polyoxometalates (POMs), as a special style of early transition metal clusters, which are usually composed of W, Mo, and V ions in their highest oxidation states and are multielectron redox active systems, have drawn intense concern due to their intriguing practical applications such as catalysis, ion exchange, electrochemistry, and so on.^{1–3} Their chirality, widely found in nature, has drawn intense concern due to not only their fascinating structural architectures but also extensive applications such as asymmetric catalysis, chiral recognition, and nonlinear optical properties.^{4–10} In light of the advantages of chirality and POMs, a great deal of effort is concentrating on the syntheses of polyoxometalate-based chiral hybrid compounds, which can integrate the functional properties of polyoxometalates and chirality. As a result of the outstanding contributions from the groups of Pope, Toshihiro, and Wang and other groups, several POM-based chiral hybrids have been obtained, most of which are molecular complexes and layered coordination polymers.^{11–17} However,

the reasonable preparation of a chiral three-dimensional (3D) POM-based MOF complex remains a great challenge.

Up to now, the preparation of POM-based chiral hybrids tended to focus upon two main methods. The first method is directly introduces chiral building blocks (chiral metal–organic moieties or chiral organic ligands) to decorate the surface of POMs.^{18,19} Therefore, the chirality can transform from these chiral units to the whole inorganic–organic hybrid framework. For example, Wang's research group obtained two new enantiomerically pure compounds with D-proline and L-proline.²⁰ The second approach to assemble chiral POM-based hybrid materials is based on self-assembly by the change of bond distances and bond angles, the formation of lacunae, structure transformation, substitution with other metals, or

Received: June 9, 2018

Accepted: August 14, 2018

Published: August 14, 2018

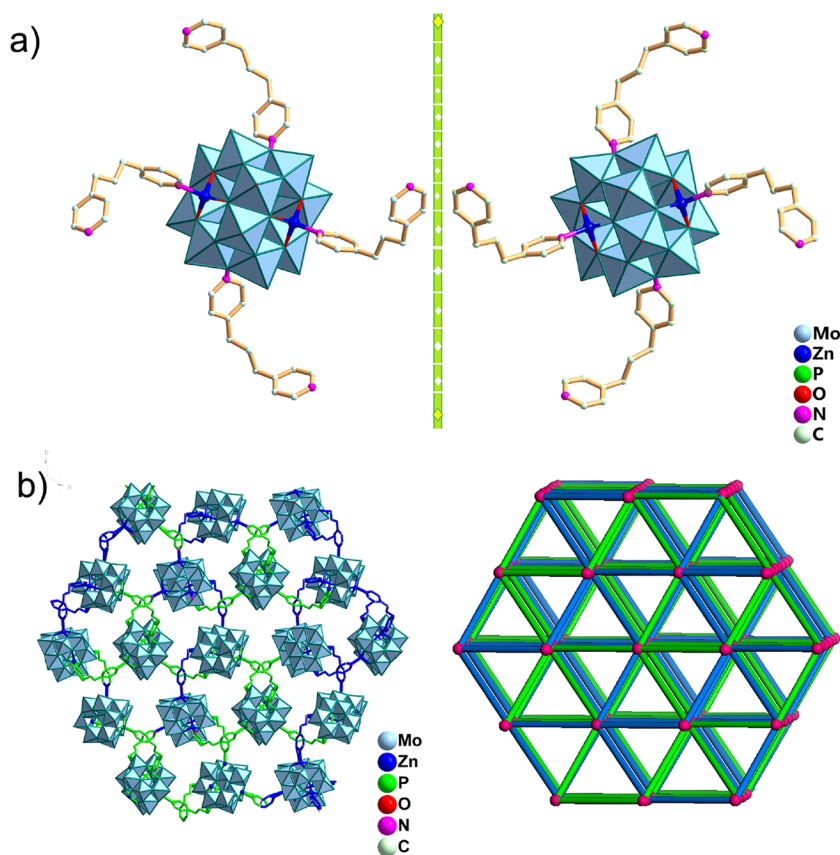


Figure 1. (a) Structural units of compounds L-1 (left) and D-1 (right) (all H atoms and guest molecules were deleted for clarity). (b) 3D frameworks of compound 1 and 2-fold interpenetrated qtz arrays, respectively.

modification with an achiral structural unit to destroy the mirror or symmetric centers.^{21–27} In this situation, chiral POM-based hybrid materials can be isolated in enantiomerically pure form by spontaneous resolution. It is very rare for spontaneous resolution phenomena and only happens occasionally.^{28–30}

Besides the methods of syntheses and novel structures of chiral POM-based compounds, their applications are also attracting significant attention from both academia and industry. Nowadays, the development of energy storage materials is a hot issue.^{31–33} Li-ion batteries (LIBs) have exhibited promising applications in energy storage.^{34–43} As a consequence, many endeavors are concentrating on exploiting the anode electrode materials with superior capacity and impressive rate capability for rechargeable LIBs. According to a recent report, in the charge and discharge process, the regular spiral conformation of the compound may offer a stable channel for charge transfer.⁴⁴ As we know, 3D chiral POM-based MOF materials, which also contain regular complex helical conformations and the redox of metal ions of POMs and provide stable charge transmission channels and oxidation–reduction center during the discharge–charge process, may show superior applications related to Li-ion rechargeable batteries. Therefore, it is meaningful to prepare chiral 3D POM-based compounds containing a spiral chain and explore their performance in Li-ion batteries.

In this work, our group chose flexible 4,4'-(1,3-propanediyl)-bipyridine (BPP) as the ligand and in situ Zn-ε-Keggin as the polyoxoanion, to self-assemble 3D chiral POM-based compounds for the following reasons: (i) The change in the BPP

ligand's configuration will lead to the lack of symmetric center, leading to chiral compounds with spiral chain. (ii) The Zn-ε-Keggin possesses a tetrahedral molecular geometry in which a central P atom is located at the center with four Zn^{II} cations located at the corners of this tetrahedron, which facilitates the formation of stable structures.^{45–49} (iii) The variable-valence redox activity of eight Mo^V and four Mo^{VI} elements in the Zn-ε-Keggin unit could provide a pathway for electrons transfer, which is beneficial to improve the performance of Li-ion battery. In the end, we succeeded in the syntheses and characterizations of two rare chiral compounds: D-[PMo₈^VMo₄^{VI}O₃₇(OH)₃Zn₄][BPP]₂·2[pyridine]·2H₂O (D-1) and L-[PMo₈^VMo₄^{VI}O₃₇(OH)₃Zn₄][BPP]₂·2[pyridine]·2H₂O (L-1). The crystal structural analyses indicate that these two kinds of coordination polymers are a pair of isomers. The substantial distinctions between compound D-1 and compound L-1 are that compound L-1 contains helical left-handed chains, while compound D-1 consists of helical right-handed chains. As far as we know, it is not easy to synthesize chiral POMOFs from achiral precursors. More importantly, no studies on chiral POMOF materials that are based on the Zn-ε-Keggin unit have been investigated. Compound 1 shows high chemical stability because it can maintain the integrity of the crystal in water solution in the pH range 2–12. When compound 1 acted as the anode of LIBs, it exhibited an initial discharge capacity of 1427 mA h g^{−1} and a steady reversible capacity of 1004 mA h g^{−1} at 100 mA g^{−1} for 100 cycles. It should be highlighted here that such a high reversible capacity has never been reported for the pristine POM-based crystals. In addition, we are the first to employ chiral POM-based 3D frameworks based on Zn-ε-

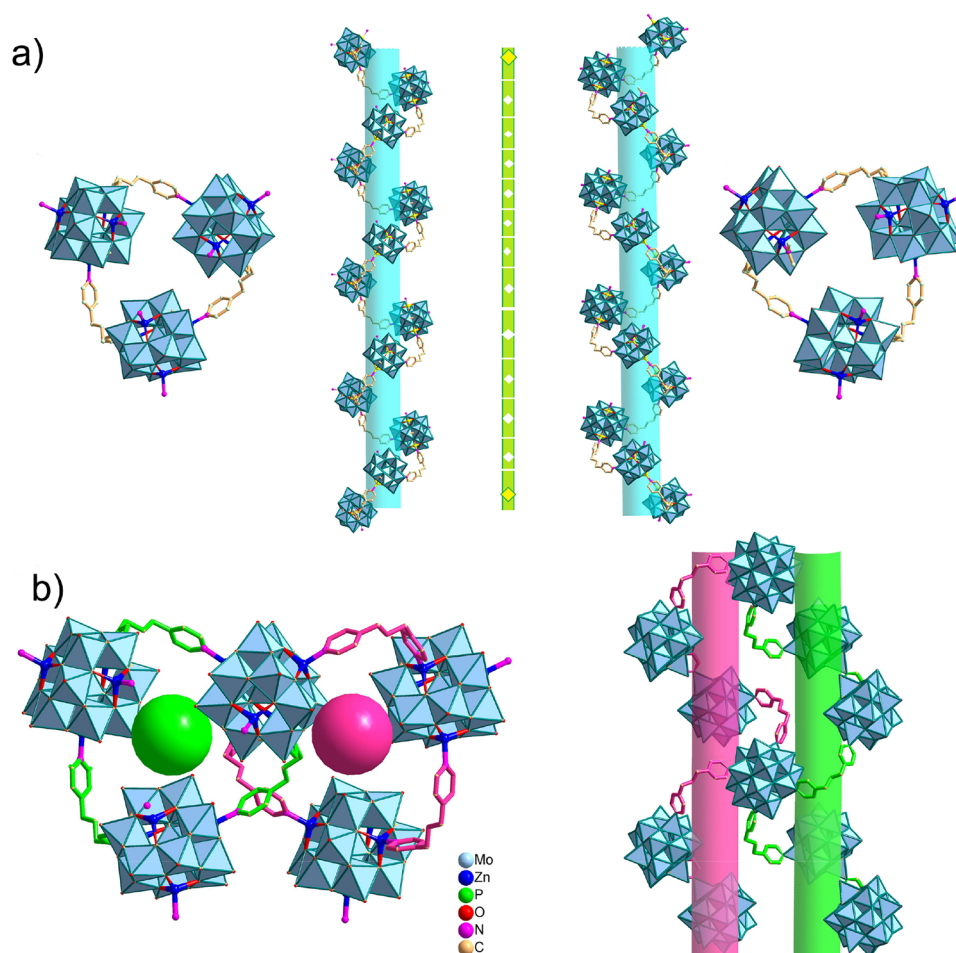


Figure 2. (a) 1D single helical chain formed by Zn1, Zn2, ϵ -keggin clusters, and BPP ligands of L-1 (left) and D-1 (right). (b) Interlocked single helical fragments sharing ϵ - $\{Zn_4PMo_{12}O_{40}\}$ ions along different directions.

Keggin units to demonstrate that the helical infinite chains and the metal-ions redox reactions of Zn- ϵ -Keggin units facilitate a boost in the performance of LIBs.

X-ray crystallography structural analyses indicate that compound D-1 and compound L-1 are a pair of optic isomers. The crystal structure of both compounds consists of half of the ϵ - $\{Zn_4PMo_{12}O_{40}\}$ ion, one BPP ligand, one guest water molecule, and one guest pyridine molecule (Figure 1a). For clarity, only the structure of compound 1 is described herein. Compound L-1 crystallizes in the trigonal crystal system, chiral space group $P\bar{3}_22_1$. In compound L-1, each Zn^{II} ion possesses tetrahedral coordination geometry, which is connected to three O atoms derived from one ϵ -Keggin unit and a N atom derived from BPP ligands. The distances of Mo–Mo have demonstrated the existence of eight Mo(V) and four Mo(VI) ions in the ϵ -Keggin cluster unit. As shown in Figure 2a (left), the Zn1 and Zn2 cations are connected by BPP ligands and the ϵ -Keggin clusters form a 1D left-handed spiral infinite chain $[-\epsilon\text{-Keggin-Zn2-BPP-Zn1-}]_n$. The main symmetry of the above helical chain is the 3_2 screw axis. Accordingly, each wall of the channel is weaved by the spiral chains. There exist completely contrary mirror images of the appropriate spiral chain in compound D-1 corresponding to those of compound L-1 (Figure 2a (right)).

Another 1D left-handed infinite helical chain $[-\epsilon\text{-Keggin-Zn1-BPP-Zn2-}]_n$ is built from Zn1 and Zn2 cations, ϵ -Keggin cluster units, and BPP ligands. One amusing aspect of

compound L-1 is that its single left-handed spiral chain originates from each other. When observed closely, the interlocked single-helical parts share ϵ - $\{Zn_4PMo_{12}O_{40}\}$ ions in the whole framework, which is different from a conventional double helix,^{50,51} allowing us to make clear the complex framework in compound L-1 (Figure 2b). As a result, an adjacent single helix is further interlinked to each other to give a regular and ordered 3D chiral architecture. From the perspective of topological structures, each Zn- ϵ -Keggin cluster is considered as a tetrahedral node and the BPP ligand as a 2-connected linker that is simplified; then the whole structure can be simplified as a 2-fold interpenetrated **qtz** net with Schläfli symbol $6^4.4.8^2$. In order to increase the steadiness of the structure and promote the generation of a small open passageway, one network is interweaved by another same **qtz** network to generate a 2-fold interpenetrated array (Figure 1b). The flack parameters are 0.032(15) for L-1 and 0.057(8) for D-1. The flack parameter values of both compounds tend to zero, which indicates that the chiral space group of both compounds is chosen correctly and the crystals are chiral.

As previously mentioned, it is very important that electrode materials have high chemical and thermal stability. As shown in Figure 3, compound 1 shows good stability when immersed in aqueous solutions with a wide pH range (1, 3, 5, 9, and 12) at room temperature. Additionally, compound 1 has good tolerance to the electrolytes of LIBs (Figure 3). The thermal stability of compound 1 has been studied by TGA analysis in

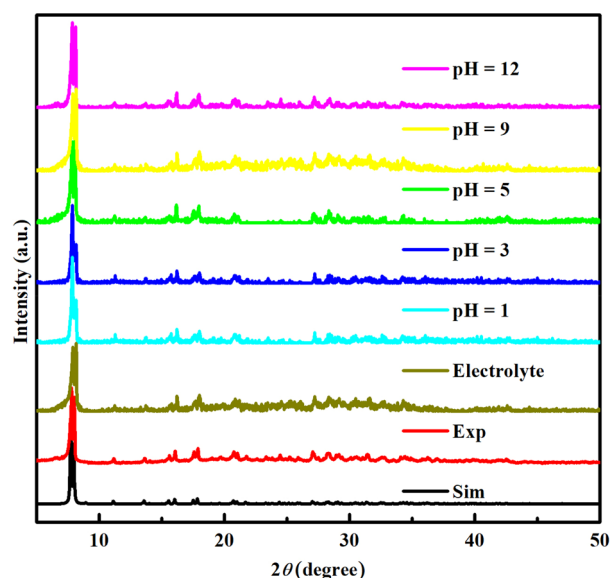


Figure 3. Power XRD patterns of compound **1**. As-synthesized compound **1** and the as-synthesized compound **1** after being immersed in a variety of pH and electrolyte conditions for 12 h at room temperature.

N_2 atmosphere. The weight loss of compound **1** from room temperature to 300 °C is 6.4% related to the releases of free water and pyridine molecules. From 306 to 836 °C, the framework gradually collapses in conformity with the splitting of all organic ligands (Supporting Information (SI) Figure S1). As shown in Figure S2, the signatures of $P=O$ and $Mo=O$ vibrations of the inorganic skeleton of the POM are encountered around 1075 and 940 cm^{-1} , respectively. The $Mo-O-Mo$ vibrations can be found below 940 cm^{-1} .

As shown in Figure S3, because of their chirality, single crystals of compound **D-1** and compound **L-1** show different colors under the polarized light, while they looked the same under natural light. Therefore, we can separate the enantiomers manually. The chiralities of compound **D-1** and compound **L-1** were further studied by circular dichroism (CD) spectra. According to the mirror images of solid state circular dichroism spectra of compound **D-1** and compound **L-1**, it is obvious that compound **D-1** and **L-1** are a pair of POM-based enantiomers. The spectra of compound **L-1** and compound **D-1** show intense Cotton effects at 206, 220, 227, and 254 nm (Figure 4).

Because $Zn-\epsilon$ -Keggin has strong redox ability and the capability to provide multielectron. In addition, the channel of MOF is beneficial to the electrolyte infiltration, which significantly increases the transport speed of Li^+ ions and electrons in the electrolyte, giving rise to a superior electrode activity. To assess their electrochemical performance, electrochemical study such as cyclic voltammetry, cycling stability, galvanostatic charge–discharge performance, and rate capability were studied. Figure 5a shows the CV curves of compound **1** at a sweep rate of 0.2 $mV s^{-1}$ in the initial four cycles. A wide cathodic signal at about 0.76 V can be seen in the first circle, which was due to the inevitable generation of the solid–electrolyte interphase (SEI) film. In the following sweep measurement, the reversible reductive and oxidative signals were observed at 0.92 and 1.30 V attributing to the oxidation–reduction process of zinc and molybdenum. The subsequent CV cycles curves almost overlap with each other,

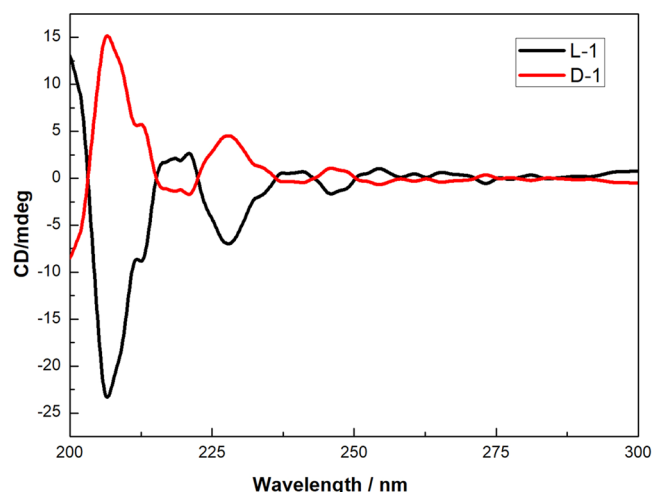


Figure 4. Circular dichroism spectra of **D-1** and **L-1**.

demonstrating superior cycle stability due to the generation of a stable SEI film. The cycling performance of compound **1** was studied at 100 $mA g^{-1}$ in the voltage range of 0.01–3.0 V versus Li/Li^+ . The charge/discharge performance together with the Coulombic efficiency (CE) of compound **1** is demonstrated in Figure 5b. Compound **1** shows high capacity with outstanding cycle stability. In pace with the charge–discharge cycles after 100 sweeps, the reversible capacity of compound **1** can be as high as 1004 $mA h g^{-1}$. To the best of knowledge, it is much higher than the previously reported POM-based materials.^{39,42,44,52} Obviously, the CE climbed substantially to almost 100% after several sweeps. As a comparative experiment, BPP ligand only delivers a reversible capacity of 193 $mA h g^{-1}$ at 100 $mA g^{-1}$ after 100 cycles. The ultrastability of compound **1** may benefit from the infinite helical chains of the chiral POMOF that could effectively accommodate the volumetric change of the polyoxometalates and succeed in averting the POMOF particles from structure damaging in the process of charging and discharging confirmed by the XRD and SEM in Figures S4 and Figure S5, in which the characteristic peaks of the XRD, structural and morphological, have hardly changed before and after cycling. Figure 5c shows the cycle numbers of 1, 10, 50, and 100 discharge–charge voltage profiles. The first reversible discharge and charge specific capacity are found to be 1427.8 and 780.9 $mA h g^{-1}$, obtaining a low CE of 54.7%. The low CE is mainly due to the inevitable electrolyte penetration and generation of a SEI layer. It is obvious that a high capacity of 842.1 $mA h g^{-1}$ was acquired in the second sweep, which increased substantially to 1004 $mA h g^{-1}$ at the 60th sweep due to the activation of the pores with convenient access of Li -ions insertion–deinsertion after consecutive cycling.

To assess its practicability, the cycling performance and rate capability performance of compound **1** were investigated at different current densities (50, 100, 200, 500, 1000, and 2000 $mA g^{-1}$). As shown in Figure 5d, the discharge capacities were 1035.8, 944.9, 846.1, 719.8, 560.9, and 379.1 $mA h g^{-1}$ at 50, 100, 200, 500, 1000, and 2000 $mA g^{-1}$, respectively. When the charge/discharge rate is back to 1000, 500, 200, 100, and 50 $mA g^{-1}$, the reversible capacities quickly recover, showing the robust rate capability of the POMOF. To further give the insight of the cyclic performance of compound **1** at the large current density, we carried out the testing at 1000 $mA g^{-1}$ with

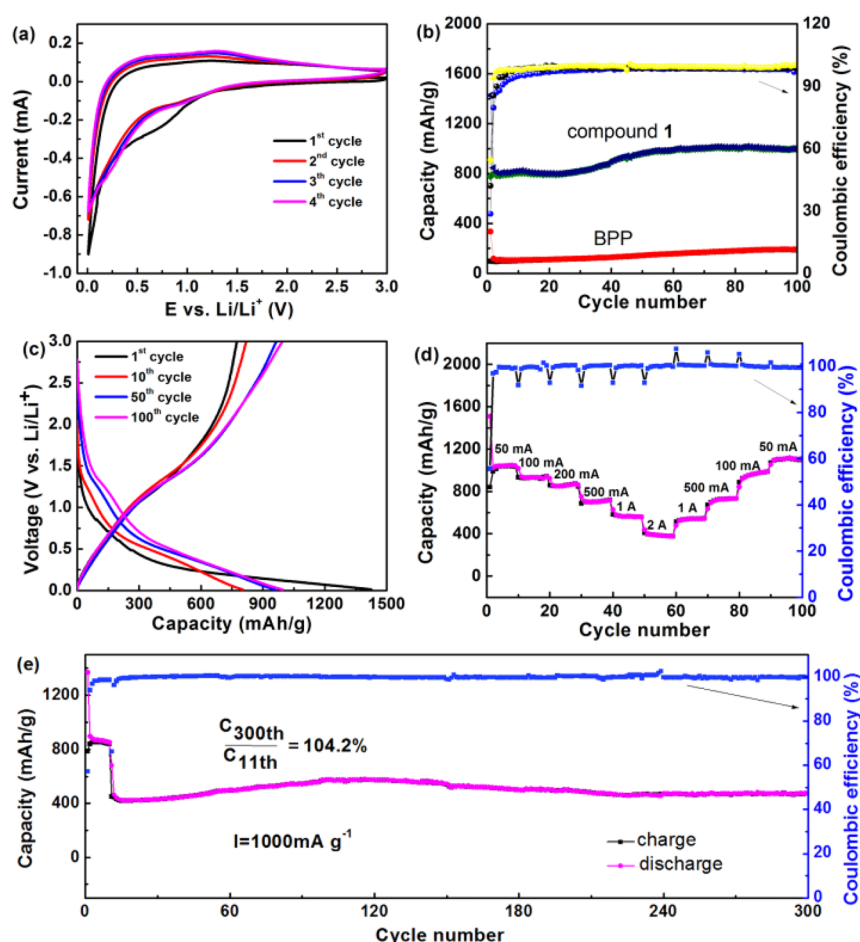


Figure 5. Electrochemical performance of compound 1 as the anode of LIBs: (a) CV profiles at a sweep rate of 0.2 mV s⁻¹. (b) Cycling performance of compound 1 and BPP at 100 mA g⁻¹. (c) The charge–discharge curves for various cycles at 100 mA g⁻¹. (d) Rate performances and Coulombic efficiencies of compound 1 at different current densities. (e) Cycling performances at 1000 mA g⁻¹ (50 mA g⁻¹ was applied to activate the electrode in the first 10 cycles).

a current density of 50 mA g⁻¹ in the first ten cycles for the activation of the electrode. The reversible capacity of compound 1 can reach as high as 469.6 mA h g⁻¹ after 300 cycles without obvious loss of capacity accompanying the capacity retention of 104.23% by comparing the capacity of the 300th cycle with the 11th cycle (Figure 5e).

To further study the contribution of elements of chiral POMOF for LIBs, the XPS survey spectrum was conducted to check the changes of valence states of the transition metal before and after discharge in the cell. The spectra indicate the carbon, molybdenum, phosphorus, zinc, and oxygen elements' existence in compound 1 (Figure S6a,e). The C 1s XPS spectrum could be assigned to three peaks [284.6 eV (C–C), 285.3 eV (C–N), and 286.5 eV (C = C)] (Figure S6b).^{53,54} After the discharge of the cell, due to the intercalation of lithium ion and the generation of the SEI (the major component is Li₂CO₃), the C=O peak replaces the C=C peak (Figure S6f). As shown in Figure S6c, the Mo 3d spectrum shows two peaks located at binding energies of 231.8 and 235.1 eV which can be deconvoluted into four peaks [Mo⁶⁺ 3d_{5/2} (232.3 eV), Mo⁶⁺ 3d_{3/2} (235.2 eV), Mo⁵⁺ 3d_{5/2} (231.1 eV), and Mo⁵⁺ 3d_{3/2} (234.2 eV)].^{38,55} However, after discharging to 0.01 V, the existence of Mo⁴⁺ can be discovered in the binding energy of 232.1 eV (Figure S6g).^{38,56} As shown in Figure S6d, two signals of Zn 2p_{3/2} (1022.5 eV) and Zn

2p_{1/2} (1045.5 eV) prove the existence of Zn²⁺, while the shifting and separation of the binding energy indicate the partial production of Zn⁰ after discharging to 0.01 V (Figure S6h).⁵⁷ Both valence changes of Mo and Zn demonstrate that the redox reactions of the ε-[Zn₄POMo₁₂O₄₀] ions occur in LIBs.

To understand the ionic and electronic transport kinetics that affect the electrochemical performance, electrochemical impedance spectroscopy (EIS) analysis has been performed (Figure S7). The Nyquist diagram showed a smaller half-circle and a sloped line in the medium- to high-frequency and low-frequency areas, respectively. R1 represents the electronic resistance of the electrolyte and electrodes. R2 represents charge transfer resistance. Warburg impedance (W₀) represents propagation of lithium ions into the solid phase. The impedance value of the compound 1 before the cycle was 179 Ω. The total resistance of compound 1 after the cycle was as low as 81 Ω demonstrating the fairly good dynamics which may be due to the fact that the flexible infinite helical chain structure of compound 1 facilitates the lithium-ion insertion/extraction and electron transmission. This is in line with the high Coulombic efficiency and the obvious improvement in rate capability performance.

The cyclic voltammograms of compound 1 at various sweep rates were performed from 0.01 to 3.0 V (Figure S8) to

confirm whether capacitance is dominated by the capacitive-controlled behavior or not based on the high reversible capacity. A power law functional relationship between current (i) and the sweep rate (v), $i = av^b$, can be used to explain this with a and b representing the alterable parameters. Under normal conditions, $b = 0.5$ signifies that the electrode reaction is diffusion-controlled and the electrode reaction satisfies Cottrell's equation, while $b = 1$ represents the reaction being restricted by a surface process. Based on the incline of the linear function graph of $\log i$ versus $\log v$, we can calculate the parameter b (Figure S9). While the scan rate gradually varied from 0.2 to 10 mV s⁻¹, the parameter b was calculated to be 0.58 at 1.1 V, signifying the main contribution of the diffusion-controlled storage process of lithium. When it comes to 0.1 V, the b value was 0.91, corresponding to the surface process. The above research proves the joint contribution of battery and capacitance performance.

The obtained high capacity and rate stability are considered to be due to the intrinsic features and the unique structure of our anode. First, Zn- ϵ -Keggin units possess high redox activity on the basis of molybdenum and zinc elements, which is good for the transfer of electrons. Second, the spiral chains of compound **1** offer good power to buffer the volume variations owing to the discharge/charge process, which offers an effective medium for charge transfer during the charging and discharging cycle. Third, the spiral chains of compound **1** guarantee more active sites contacting the point of lithium ion and electrolyte guaranteeing the rapid transfer of electrons in the electrode. All these unique chemical and physical properties of POMOF are beneficial to the superior electrochemical performance of the anode of LIBs.

In summary, we designed and prepared unprecedented stable chiral three-dimensional POM-based MOF materials constructed by achiral BPP ligands and Zn- ϵ -Keggin units with excellent chemical stability in reagents with various pH and electrolytes. Furthermore, compound **1** exhibits splendid electrochemical activity as the anode of LIBs, acquiring a reversible capacitance of 1004 mA h g⁻¹ at 100 mA h g⁻¹ after 100 cycles with impressive rate performance. Such a high reversible capacity has previously never been reported for the LIB anodes within the pristine POM-based crystals. This excellent performance can be ascribed to its flexible infinite helical chain structure facilitating the lithium-ions insertion/extraction, electron transmission, and buffering the volume changes during charge and discharge. What's more, we first employed the chiral three-dimensional POMOF crystalline feature to demonstrate that the spiral chains structure and the redox active center of metal ions in POMs are helpful to greatly enhance the properties of LIBs, which might indicate a direction for the design and preparation of novel anode materials in relation to chiral materials with spiral chains for future development in LIBs material.

■ ASSOCIATED CONTENT

■ Supporting Information

The Supporting Information is available free of charge on the ACS Publications website at DOI: 10.1021/acsaeam.8b00938.

Synthesis, single-crystal structure analysis, characterization, supplementary structural figures, PXRD measurements, IR spectrum, and XPS analysis, and comparison of compound **1** with other pristine anode materials (PDF)

Crystallographic data for compound D-1 (CIF)

Crystallographic data for compound L-1 (CIF)

■ AUTHOR INFORMATION

Corresponding Authors

*(Y.X.) E-mail: yanxu@njtech.edu.cn.

*(Y.-Q.L.) E-mail: yqlan@njnu.edu.cn.

ORCID

Ya-Qian Lan: 0000-0002-2140-7980

Yan Xu: 0000-0001-6059-075X

Author Contributions

[†]W.C. and F.-C.S. contributed equally to this work.

Notes

The authors declare no competing financial interest.

■ ACKNOWLEDGMENTS

This work was supported by the NSFC (Grant 21571103), the Natural Science Foundation of Jiangsu Province, China (Grant BK2012823), and the Qing Lan project.

■ REFERENCES

- (1) Dolbecq, A.; Dumas, E.; Mayer, C. R.; Mialane, P. Hybrid Organic-Inorganic Polyoxometalate Compounds: From Structural Diversity to Applications. *Chem. Rev.* **2010**, *110*, 6009–6048.
- (2) Dini, D.; Calvete, M. J. F.; Hanack, M. Nonlinear Optical Materials for the Smart Filtering of Optical Radiation. *Chem. Rev.* **2016**, *116*, 13043–13233.
- (3) Zhou, E.-L.; Qin, C.; Wang, X.-L.; Shao, K.-Z.; Su, Z.-M. Assembly of two novel 3D organic-inorganic hybrids based on Keggin-type polyoxometalates: syntheses, crystal structures and properties. *CrystEngComm* **2016**, *18*, 6370–6377.
- (4) Wu, X.; Zhang, H.-B.; Xu, Z.-X.; Zhang, J. Asymmetric induction in homochiral MOFs: from interweaving double helices to single helices. *Chem. Commun.* **2015**, *51*, 16331–16333.
- (5) Han, Q.; He, C.; Zhao, M.; Qi, B.; Niu, J.; Duan, C. Engineering Chiral Polyoxometalate Hybrid Metal–Organic Frameworks for Asymmetric Dihydroxylation of Olefins. *J. Am. Chem. Soc.* **2013**, *135*, 10186–10189.
- (6) Prins, L. J.; Huskens, J.; de Jong, F.; Timmerman, P.; Reinhoudt, D. N. Complete asymmetric induction of supramolecular chirality in a hydrogen-bonded assembly. *Nature* **1999**, *398*, 498.
- (7) Song, F.; Wang, C.; Falkowski, J. M.; Ma, L.; Lin, W. Isorecticular Chiral Metal–Organic Frameworks for Asymmetric Alkene Epoxidation: Tuning Catalytic Activity by Controlling Framework Catenation and Varying Open Channel Sizes. *J. Am. Chem. Soc.* **2010**, *132*, 15390–15398.
- (8) Tan, H.; Li, Y.; Zhang, Z.; Qin, C.; Wang, X.; Wang, E.; Su, Z. Chiral Polyoxometalate-Induced Enantiomerically 3D Architectures: A New Route for Synthesis of High-Dimensional Chiral Compounds. *J. Am. Chem. Soc.* **2007**, *129*, 10066–10067.
- (9) Zhou, M.; Yan, D.; Dong, Y.; He, X.; Xu, Y. Chiral [Mo8O26]4- Polyoxoanion-Induced Three-Dimensional Architectures With Homochiral Eight-Fold Interpenetrated Metal–Organic Frameworks. *Inorg. Chem.* **2017**, *56*, 9036–9043.
- (10) Song, B.-Q.; Chen, D.-Q.; Ji, Z.; Tang, J.; Wang, X.-L.; Zang, H.-Y.; Su, Z.-M. Control of bulk homochirality and proton conductivity in isostructural chiral metal-organic frameworks. *Chem. Commun.* **2017**, *53*, 1892–1895.
- (11) Qin, C.; Wang, X.-L.; Yuan, L.; Wang, E.-B. Chiral Self-Threading Frameworks Based on Polyoxometalate Building Blocks Comprising Unprecedented Tri-Flexure Helix. *Cryst. Growth Des.* **2008**, *8*, 2093–2095.
- (12) Fang, X.; Anderson, T. M.; Hou, Y.; Hill, C. L. Stereoisomerism in polyoxometalates: structural and spectroscopic studies of bis-

(malate)-functionalized cluster systems. *Chem. Commun.* **2005**, *40*, 5044–5046.

(13) Kortz, U.; Savelieff, M. G.; Ghali, F. Y. A.; Khalil, L. M.; Maalouf, S. A.; Sinno, D. I. Mit Aminosäuren funktionalisierte Heteropolymolybdate von AsIII, SbIII, BiIII, SeIV und TeIV. *Angew. Chem.* **2002**, *114*, 4246–4249.

(14) Miyao, I.; Toshihiro, Y. Crystal Structure of the Pentamolybdate Complex Coordinated by Adenosine-5'-monophosphoric Acid. *Bull. Chem. Soc. Jpn.* **1996**, *69*, 2863–2868.

(15) Xin, F.; Pope, M. T. Lone-Pair-Induced Chirality in Polyoxotungstate Structures: Tin(II) Derivatives of A-Type XW₉O₃₄n- (X = P, Si). Interaction with Amino Acids. *J. Am. Chem. Soc.* **1996**, *118*, 7731–7736.

(16) Xiao, F.; Hao, J.; Zhang, J.; Lv, C.; Yin, P.; Wang, L.; Wei, Y. Polyoxometalacyclophanes: Controlled Assembly of Polyoxometalate-Based Chiral Metallamacrocycles from Achiral Building Blocks. *J. Am. Chem. Soc.* **2010**, *132*, 5956–5957.

(17) Long, D.-L.; Kögerler, P.; Farrugia, L. J.; Cronin, L. Linking Chiral Clusters with Molybdate Building Blocks: From Homochiral Helical Supramolecular Arrays to Coordination Helices. *Chem. - Asian J.* **2006**, *1*, 352–357.

(18) Ishimoto, R.; Kamata, K.; Suzuki, K.; Yamaguchi, K.; Mizuno, N. Synthesis and structural characterization of BINOL-modified chiral polyoxometalates. *Dalton Trans* **2015**, *44*, 10947–10951.

(19) Zhuo, C.; Wen, Y.; Wu, X. Strategies to construct homochiral metal-organic frameworks: ligands selection and practical techniques. *CrystEngComm* **2016**, *18*, 2792–2802.

(20) An, H.-Y.; Wang, E.-B.; Xiao, D.-R.; Li, Y.-G.; Su, Z.-M.; Xu, L. Chiral 3D Architectures with Helical Channels Constructed from Polyoxometalate Clusters and Copper–Amino Acid Complexes. *Angew. Chem., Int. Ed.* **2006**, *45*, 904–908.

(21) Shyu, E.; Supkowski, R. M.; LaDuca, R. L. A Chiral Luminescent Coordination Polymer Featuring a Unique 4-Connected Self-Catenated Topology Built from Helical Motifs. *Inorg. Chem.* **2009**, *48*, 2723–2725.

(22) Zhang, J.; Luo, J.; Wang, P.; Ding, B.; Huang, Y.; Zhao, Z.; Zhang, J.; Wei, Y. Step-by-Step Strategy from Achiral Precursors to Polyoxometalates-Based Chiral Organic–Inorganic Hybrids. *Inorg. Chem.* **2015**, *54*, 2551–2559.

(23) Zhang, J.; Hao, J.; Wei, Y.; Xiao, F.; Yin, P.; Wang, L. Nanoscale Chiral Rod-like Molecular Triads Assembled from Achiral Polyoxometalates. *J. Am. Chem. Soc.* **2010**, *132*, 14–15.

(24) Zhang, J.; Chen, S.; Valle, H.; Wong, M.; Austria, C.; Cruz, M.; Bu, X. Manganese and Magnesium Homochiral Materials: Decoration of Honeycomb Channels with Homochiral Chains. *J. Am. Chem. Soc.* **2007**, *129*, 14168–14169.

(25) Hou, Y.; An, H.; Xu, T.; Zhao, S.; Luo, J. Chiral polyoxomolybdate-based hybrid compounds obtained by spontaneous resolution: syntheses, structures and non-linear optical properties. *New J. Chem.* **2016**, *40*, 10316–10324.

(26) Zhao, X.; He, H.; Dai, F.; Sun, D.; Ke, Y. Supramolecular Isomerism in Honeycomb Metal–Organic Frameworks Driven by CH $\cdots\pi$ Interactions: Homochiral Crystallization from an Achiral Ligand through Chiral Inducement. *Inorg. Chem.* **2010**, *49*, 8650–8652.

(27) Prabhakar, M.; Zacharias, P. S.; Das, S. K. Self-Assembly of a Fluorescent Chiral Zinc(II) Complex That Leads to Supramolecular Helices. *Inorg. Chem.* **2005**, *44*, 2585–2587.

(28) An, H.; Wang, L.; Hu, Y.; Xu, T.; Hou, Y. Spontaneous Resolution of Evans–Showell-Type Polyoxometalates in Constructing Chiral Inorganic–Organic Hybrid Architectures. *Inorg. Chem.* **2016**, *55*, 144–153.

(29) Xue, Y.-S.; Tan, X.; Zhou, M.; Mei, H.; Xu, Y. Synthesis, structures and magnetic properties of two chiral mixed-valence iron(ii,iii) coordination networks. *Dalton Trans* **2017**, *46*, 16623–16630.

(30) Tang, Q.; Liu, S.; Liu, Y.; Li, S.; Ma, F.; Li, J.; Wang, S.; Liu, C. Assembly and spontaneous resolution of the chiral inorganic

polyoxometalates-based frameworks via helical chains association. *Dalton Trans* **2013**, *42*, 8512–8518.

(31) Palomares, V.; Serras, P.; Villaluenga, I.; Hueso, K. B.; Carretero-Gonzalez, J.; Rojo, T. Na-ion batteries, recent advances and present challenges to become low cost energy storage systems. *Energy Environ. Sci.* **2012**, *5*, 5884–5901.

(32) Larcher, D.; Tarascon, J. M. Towards greener and more sustainable batteries for electrical energy storage. *Nat. Chem.* **2015**, *7*, 19–29.

(33) Pan, H.; Hu, Y.-S.; Chen, L. Room-temperature stationary sodium-ion batteries for large-scale electric energy storage. *Energy Environ. Sci.* **2013**, *6*, 2338–2360.

(34) Gong, T.; Lou, X.; Gao, E.-Q.; Hu, B. Pillared-Layer Metal–Organic Frameworks for Improved Lithium-Ion Storage Performance. *ACS Appl. Mater. Interfaces* **2017**, *9*, 21839–21847.

(35) Li, C.; Lou, X.; Shen, M.; Hu, X.; Guo, Z.; Wang, Y.; Hu, B.; Chen, Q. High Anodic Performance of Co_{1.3},5-Benzenetricarboxylate Coordination Polymers for Li-Ion Battery. *ACS Appl. Mater. Interfaces* **2016**, *8*, 15352–15360.

(36) Wang, L.; He, X.; Li, J.; Sun, W.; Gao, J.; Guo, J.; Jiang, C. Nano-Structured Phosphorus Composite as High-Capacity Anode Materials for Lithium Batteries. *Angew. Chem., Int. Ed.* **2012**, *51*, 9034–9037.

(37) Chen, X.; Wang, Z.; Zhang, R.; Xu, L.; Sun, D. A novel polyoxometalate-based hybrid containing a 2D [CoMo₈O₂₆]-[infinity] structure as the anode for lithium-ion batteries. *Chem. Commun.* **2017**, *53*, 10560–10563.

(38) Li, X.-X.; Shen, F.-C.; Liu, J.; Li, S.-L.; Dong, L.-Z.; Fu, Q.; Su, Z.-M.; Lan, Y.-Q. A highly stable polyoxometalate-based metal-organic framework with an ABW zeolite-like structure. *Chem. Commun.* **2017**, *53*, 10054–10057.

(39) Huang, Q.; Wei, T.; Zhang, M.; Dong, L.-Z.; Zhang, A. M.; Li, S.-L.; Liu, W.; Liu, J.; Lan, Y.-Q. A highly stable polyoxometalate-based metal-organic framework with [small pi]-[small pi] stacking for enhancing performance in lithium ion battery. *J. Mater. Chem. A* **2017**, *5*, 8477–8483.

(40) Liu, Q.; Yu, L.; Wang, Y.; Ji, Y.; Horvat, J.; Cheng, M.-L.; Jia, X.; Wang, G. Manganese-Based Layered Coordination Polymer: Synthesis, Structural Characterization, Magnetic Property, and Electrochemical Performance in Lithium-Ion Batteries. *Inorg. Chem.* **2013**, *52*, 2817–2822.

(41) Yang, X.-Y.; Wei, T.; Li, J.-S.; Sheng, N.; Zhu, P.-P.; Sha, J.-Q.; Wang, T.; Lan, Y.-Q. Polyoxometalate-Incorporated Metallapillararene/Metallacalixarene Metal-Organic Frameworks as Anode Materials for Lithium Ion Batteries. *Inorg. Chem.* **2017**, *56*, 8311–8318.

(42) Yue, Y.; Li, Y.; Bi, Z.; Veith, G. M.; Bridges, C. A.; Guo, B.; Chen, J.; Mullins, D. R.; Surwade, S. P.; Mahurin, S. M.; Liu, H.; Paranthaman, M. P.; Dai, S. A POM-organic framework anode for Li-ion battery. *J. Mater. Chem. A* **2015**, *3*, 22989–22995.

(43) Wei, T.; Zhang, M.; Wu, P.; Tang, Y.-J.; Li, S.-L.; Shen, F.-C.; Wang, X.-L.; Zhou, X.-P.; Lan, Y.-Q. POM-based metal-organic framework/reduced graphene oxide nanocomposites with hybrid behavior of battery-supercapacitor for superior lithium storage. *Nano Energy* **2017**, *34*, 205–214.

(44) Li, M.; Cong, L.; Zhao, J.; Zheng, T.; Tian, R.; Sha, J.; Su, Z.; Wang, X. Self-organization towards complex multi-fold meso-helices in the structures of Wells–Dawson polyoxometalate-based hybrid materials for lithium-ion batteries. *J. Mater. Chem. A* **2017**, *5*, 3371–3376.

(45) Marleny Rodriguez-Albelo, L.; Ruiz-Salvador, A. R.; Sampieri, A.; Lewis, D. W.; Gómez, A.; Nohra, B.; Mialane, P.; Marrot, J.; Sécheresse, F.; Mellot-Draznieks, C.; Ngo Biboum, R.; Keita, B.; Nadjo, L.; Dolbecq, A. Zeolitic Polyoxometalate-Based Metal–Organic Frameworks (Z-POMOFs): Computational Evaluation of Hypothetical Polymorphs and the Successful Targeted Synthesis of the Redox-Active Z-POMOF1. *J. Am. Chem. Soc.* **2009**, *131*, 16078–16087.

(46) Nohra, B.; El Moll, H.; Rodriguez Albelo, L. M.; Mialane, P.; Marrot, J.; Mellot-Draznieks, C.; O'Keeffe, M.; Ngo Biboum, R.;

Lemaire, J.; Keita, B.; Nadjio, L.; Dolbecq, A. Polyoxometalate-Based Metal Organic Frameworks (POMOFs): Structural Trends, Energetics, and High Electrocatalytic Efficiency for Hydrogen Evolution Reaction. *J. Am. Chem. Soc.* **2011**, *133*, 13363–13374.

(47) Qin, J. S.; Du, D. Y.; Guan, W.; Bo, X. J.; Li, Y. F.; Guo, L. P.; Su, Z. M.; Wang, Y. Y.; Lan, Y. Q.; Zhou, H. C. Ultrastable Polymolybdate-Based Metal Organic Frameworks as Highly Active Electrocatalysts for Hydrogen Generation from Water. *J. Am. Chem. Soc.* **2015**, *137*, 7169–7177.

(48) Lei, C.; Mao, J.-G.; Sun, Y.-Q.; Song, J.-L. A Novel Organic–Inorganic Hybrid Based on an 8-Electron-Reduced Keggin Polymolybdate Capped by Tetrahedral, Trigonal Bipyramidal, and Octahedral Zinc: Synthesis and Crystal Structure of $(\text{CH}_3\text{NH}_3)(\text{H}_2\text{bipy})[\text{Zn}_4(\text{bipy})_3(\text{H}_2\text{O})_2\text{MoV}_8\text{MoVI}_4\text{O}_{36}(\text{PO}_4)] \cdot 4\text{H}_2\text{O}$. *Inorg. Chem.* **2004**, *43*, 1964–1968.

(49) Rodriguez-Albelo, L. M.; Rousseau, G.; Mialane, P.; Marrot, J.; Mellot-Draznieks, C.; Ruiz-Salvador, A. R.; Li, S.; Liu, R.; Zhang, G.; Keita, B.; Dolbecq, A. γ -Keggin-based coordination networks: Synthesis, structure and application toward green synthesis of polyoxometalate@graphene hybrids. *Dalton Trans* **2012**, *41*, 9989–9999.

(50) Cordes, D. B.; Hanton, L. R.; Spicer, M. D. Helices versus Zigzag Chains: One-Dimensional Coordination Polymers of AgI and Bis(4-pyridyl)amine. *Inorg. Chem.* **2006**, *45*, 7651–7664.

(51) Liu, S.; Li, L.-L.; Li, H.; Gao, H.-L.; Cui, J.-Z.; Cheng, P. Slow magnetic relaxation in a lanthanide helix chain compound $[\text{Dy}(\text{HNA})(\text{NA})_2(\text{NO}_3)]_n$ (HNA = nicotinic acid). *Dalton Trans* **2015**, *44*, 6169–6174.

(52) Wang, Y.-Y.; Zhang, M.; Li, S.-L.; Zhang, S.-R.; Xie, W.; Qin, J.; Su, Z.-M.; Lan, Y.-Q. Diamondoid-Structured Polymolybdate-Based Metal-Organic Framework as a High-Capacity Anode for Lithium-Ion Batteries. *Chem. Commun.* **2017**, *53*, 5204–5207.

(53) Govindhan, M.; Mao, B.; Chen, A. Novel cobalt quantum dot/graphene nanocomposites as highly efficient electrocatalysts for water splitting. *Nanoscale* **2016**, *8*, 1485–1492.

(54) Shen, F.-C.; Wang, Y.; Tang, Y.-J.; Li, S.-L.; Wang, Y.-R.; Dong, L.-Z.; Li, Y.-F.; Xu, Y.; Lan, Y.-Q. CoV_2O_6 – V_2O_5 Coupled with Porous N-Doped Reduced Graphene Oxide Composite as a Highly Efficient Electrocatalyst for Oxygen Evolution. *ACS Energy Letters* **2017**, *2*, 1327–1333.

(55) Xie, J.; Zhang, Y.; Han, Y.; Li, C. High-Capacity Molecular Scale Conversion Anode Enabled by Hybridizing Cluster-Type Framework of High Loading with Amino-Functionalized Graphene. *ACS Nano* **2016**, *10*, 5304–5313.

(56) Xia, F.; Hu, X.; Sun, Y.; Luo, W.; Huang, Y. Layer-by-layer assembled MoO_2 -graphene thin film as a high-capacity and binder-free anode for lithium-ion batteries. *Nanoscale* **2012**, *4*, 4707–4711.

(57) Nakamura, J.; Nakamura, I.; Uchijima, T.; Kanai, Y.; Watanabe, T.; Saito, M.; Fujitani, T. A Surface Science Investigation of Methanol Synthesis over a Zn-Deposited Polycrystalline Cu Surface. *J. Catal.* **1996**, *160*, 65–75.